PHYSICAL REVIEW APPLIED **13,** 064006 (2020)

Tunable Magnetoresistance and Charge Carrier Density in $Cr{:}In_2O_3/PbMg_{1/3}Nb_{2/3}O_3$-$PbTiO_3$ Ferroelectric Field-Effect Devices

Meng Xu,[1,2] Ting-Wei Chen,[3] Jian-Min Yan,[1] Lei Guo,[1] Hui Wang,[3] Guan-Yin Gao,[4,*] Hao-Su Luo,[1]
Yang Chai,[5] and Ren-Kui Zheng[1,3,†]

[1] *State Key Laboratory of High Performance Ceramics and Superfine Microstructure, Shanghai Institute of Ceramics, Chinese Academy of Sciences, Shanghai 200050, China*
[2] *Center of Materials Science and Optoelectronics Engineering, University of Chinese Academy of Sciences, Beijing 100049, China*
[3] *School of Materials Science and Engineering, Jiangxi Engineering Laboratory for Advanced Functional Thin Films, Nanchang University, Nanchang 330031, China*
[4] *Hefei National Laboratory for Physical Sciences, University of Science and Technology of China, Hefei 230026, China*
[5] *Department of Applied Physics, The Hong Kong Polytechnic University, Hung Hom, Hong Kong, China*

(Received 4 February 2020; revised manuscript received 19 April 2020; accepted 27 April 2020; published 2 June 2020)

We report the epitaxial growth of the Cr-doped $In_{2-x}Cr_xO_3$ ($x = 0.05$) ($Cr{:}In_2O_3$) semiconducting thin films on perovskite-type (111)-oriented $0.7Pb(Mg_{1/3}Nb_{2/3})O_3-0.3PbTiO_3$ (PMN-PT) ferroelectric single-crystal substrates in the form of ferroelectric field-effect devices that allow us to obtain an *in situ* tuning of the electron carrier density and magnetoresistance (MR) as well as the resistance in a reversible and nonvolatile manner, thereby stringently disclosing the relationship between the MR and the electron carrier density. Specifically, for the thinnest 25-nm $Cr{:}In_2O_3$ film the polarization switching of the PMN-PT from the positively polarized P_r^+ state to the negatively polarized P_r^- state results in a large increase in the resistance and MR. Particularly, at $T = 10$ K, the polarization switching induces reversible and nonvolatile changes in the magnitude and sign of MR, demonstrating strong coupling between the MR and the electron carrier density. Moreover, regardless of the polarization states of PMN-PT, MR for films with different thicknesses can be quite well described by a combination of the two-band model and the semiempirical model proposed by Khosla and Fischer based on which the positive MR (PMR) and negative MR (NMR) could be disentangled into positive component [MR(+)] and negative component [MR(−)], respectively. We find that the polarization-switching-induced large decrease in the PMR and the change in the sign of MR from positive to negative is mainly due to the rapid decrease in the MR(+), demonstrating that the coupling between MR(+) and electron carrier density plays a dominant role in controlling the magnitude and sign of MR.

DOI: 10.1103/PhysRevApplied.13.064006

I. INTRODUCTION

Indium oxide (In_2O_3) is a wide band-gap semiconductor with a direct band gap of 2.63 eV [1] and has been extensively studied for many emerging device applications such as transparent electronics, light-emitting diodes, smart windows, and chemical gas sensors [2–4]. In addition, the observation of room-temperature ferromagnetism and giant magnetoresistance (MR) in transition-metal-(TM) doped In_2O_3 thin films makes them promising materials for spintronic device applications [5,6]. Here, the MR is defined as $MR = [R(H) - R(0)]/R(0)$, where $R(H)$ and $R(0)$ are the resistance of the TM-doped In_2O_3 films in the presence and absence of a magnetic field H, respectively. Unfortunately, the MR behaviors and their underlining mechanisms are complicated and controversial in different reports [5–15]. The positive MR (PMR) in TM-doped wide band-gap-semiconductor thin films is usually attributed to the *s-d* exchange interaction-induced spin-splitting effect [5,7–9] while the negative MR (NMR) is commonly ascribed to the spin-dependent scattering as a result of the formation of magnetic polarons [5,7,8,10]. In addition, other mechanisms have also been proposed to understand MR behaviors. For instance, some researchers believe that the PMR arises from the action of Lorentz force on the mobile carriers [11,12]. In the variable-range-hopping (VRH) regime, where the charge carrier hopping distance is relatively large, the giant PMR could originate from

---

[*] ggy@ustc.edu.cn
[†] zrk@ustc.edu

2331-7019/20/13(6)/064006(11)

the shrinking of the wave functions of the states available for an electron hop [6,13,14]. For systems in the weakly localized regime, some researchers attribute the NMR to the magnetic-field-induced suppression of the weak localization effect [9,15]. There is no doubt that all of these mechanisms are closely correlated to the film's charge carrier density, which is one of the core factors that affects the resistance, MR, and the device's performance [5–9,11,15]. Therefore, researchers usually study MR behaviors and related mechanisms by regulating the charge carrier density of films through changing the types and contents of doped transition-metal elements and the film's preparation conditions such as the growing and annealing oxygen pressures and substrate temperatures [6–10,15]. However, by these means, unfavorable factors that also affect MR behaviors of thin films will inevitably be introduced, such as the uneven distribution of doped transition-metal ions and variation of defects, disorders, crystalline quality from sample to sample. This may be one of the reasons that lead to distinct MR behaviors even for thin films prepared with similar compositions. Therefore, it is highly desired that the MR behaviors could be *in situ* reversibly modulated in a nonvolatile manner by simply modifying the charge carrier density while keeping aforementioned unfavorable factors constant. In this context, we note that ferroelectric field-effect transistors (FE FETs) in the form of thin-film and ferroelectric structures can be exploited for this purpose [16–20]. Among diverse ferroelectrics, perovskite-type $(1-x)\mathrm{Pb(Mg_{1/3}Nb_{2/3})O_3}-x\mathrm{PbTiO_3}$ single crystals with the $\mathrm{PbTiO_3}$ composition near the morphotropic phase boundary are well favored due to their large remnant polarization ($P_r \approx 40\ \mu\mathrm{C/cm^2}$, corresponding to a large areal surface-polarization charge of approximately $2.5 \times 10^{14}/\mathrm{cm^2}$) and extremely small leakage current density ($<10^{-9}\ \mathrm{A/cm^2}$) at room temperature [21,22]. It is expected that the integration of TM-doped $\mathrm{In_2O_3}$ films with $(1-x)\mathrm{Pb(Mg_{1/3}Nb_{2/3})O_3}-x\mathrm{PbTiO_3}$ could not only realize a reversible and nonvolatile modulation of the electron carrier density and MR behaviors of TM-doped $\mathrm{In_2O_3}$ films, but also provide an elaborate framework for exploring intrinsic carrier-density-related properties of semiconductor films and potential applications of semiconductor-ferroelectric FE FETs.

Based on the above considerations we fabricate Cr-doped $\mathrm{In_2O_3}$ ($\mathrm{Cr{:}In_2O_3}$) epitaxial films with different thicknesses on the $0.7\mathrm{Pb(Mg_{1/3}Nb_{2/3})O_3}-0.3\mathrm{PbTiO_3}$ (PMN-PT) single-crystal substrates and systematically studied the effects of the ferroelectric field effect, film thickness, and temperature on the MR behaviors and related mechanisms for the $\mathrm{Cr{:}In_2O_3}$ films. Our results not only gain a comprehensive and deeper insight into the intrinsic relationship between MR and electron carrier density, but also pave a way toward the nonvolatile spintronic devices in the form of semiconductor and ferroelectric hybrid structures.

II. EXPERIMENTAL DETAILS

The Cr-doped $\mathrm{In_{2\text{-}x}Cr_xO_3}$ ($\mathrm{Cr{:}In_2O_3}$) films with nominal doping level of $x = 0.05$ are grown on one-side-polished (111)-oriented PMN-PT single-crystal substrates by the pulse laser deposition using a KrF excimer laser ($\lambda = 248$ nm) with an energy density of 1.5 $\mathrm{J/cm^2}$ and a repetition rate of 3 Hz. During film deposition the oxygen pressure and substrate temperature are kept at 25 Pa and 600 °C, respectively. The distance between the $\mathrm{Cr{:}In_2O_3}$ target and the PMN-PT substrates is 5 cm. The as-grown $\mathrm{Cr{:}In_2O_3}$ films are cooled to room temperature at a rate of 5 °C/min. The film thickness is controlled by the number of laser pulses.

The crystallographic properties of $\mathrm{Cr{:}In_2O_3}$ films are characterized by XRD $\theta - 2\theta$ and φ scans using a x-ray diffractometer (PANalytical X'Pert PRO) equipped with Cu $K\alpha_1$ radiation ($\lambda = 1.5406$ Å). The film thickness is measured by a field-emission scanning electron microscope (SU8220 FE-SEM). The film composition is examined using an energy-dispersive x-ray spectrometer (EDS) (Oxford Aztec X-Max80) installed on a Zeiss Supra 55 scanning electron microscope. The cross-section HRTEM image is measured using a Tecnai G2F20 S-Twin transmission electron microscope.

Before electronic transport measurements Ag films with a thickness of approximately 100 nm are deposited onto the top of the $\mathrm{Cr{:}In_2O_3}$ films and the bottom of PMN-PT substrates by the ion sputtering method. It should be noted that the strip aluminum foils are placed on the $\mathrm{Cr{:}In_2O_3}$ films other than the four electrode positions when the Ag films are deposited onto the top of the $\mathrm{Cr{:}In_2O_3}$ films. After the removal of the strip aluminum foils, four silver film electrodes are formed on the top of the $\mathrm{Cr{:}In_2O_3}$ film. The electric field is applied to the PMN-PT substrates along the thickness direction through the conducting $\mathrm{Cr{:}In_2O_3}$ film and the bottom Ag electrodes [the inset of Fig. 2(a)]. Room-temperature resistance switching upon the application of bipolar electric fields is measured using a Keithley 2400 source meter and a Keithley 2000 multimeter. The Hall effect and resistance of the $\mathrm{Cr{:}In_2O_3}$ films are measured using a Physical Property Measurement System (PPMS-9, Quantum Design) via the Van der Pauw method and the four-probe method, respectively. The charge carrier density and magnetoresistance can be calculated from the Hall effect and resistance measurement results, respectively.

III. RESULTS AND DISCUSSION

Figure 1(a) shows the XRD θ–2θ scan patterns for all of the $\mathrm{Cr{:}In_2O_3}$/PMN-PT structures. The presence of only (*lll*) reflections implies single-phase and (111)-oriented growth of the $\mathrm{Cr{:}In_2O_3}$ films. The average crystallite size of the $\mathrm{Cr{:}In_2O_3}$ films estimated by Scherrer's equation from the intensity of the half-maximum

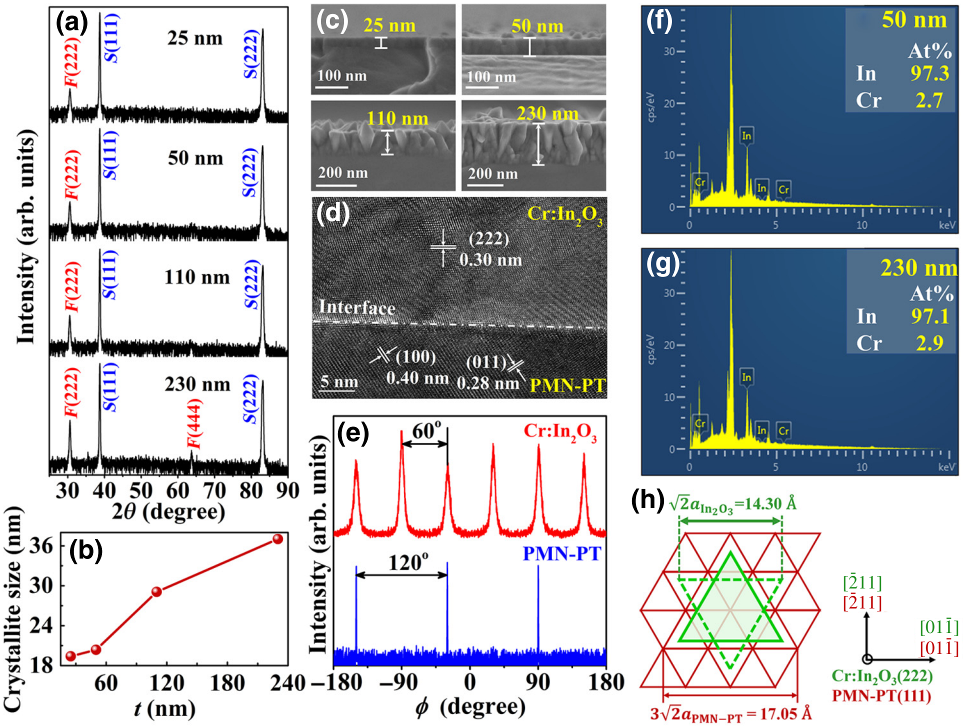

FIG. 1. (a) XRD $\theta-2\theta$ scan patterns for the $Cr:In_2O_3$/PMN-PT structures. (b) The average crystallite size of the $Cr:In_2O_3$ films estimated by Scherrer's equation. (c) Cross-section SEM images of $Cr:In_2O_3$/PMN-PT structures with film thickness ranging from 25 to 230 nm. (d) Cross-section HRTEM image of the 230-nm $Cr:In_2O_3$/PMN-PT structure. (e) XRD ϕ scan patterns taken on the $Cr:In_2O_3$ (400) and PMN-PT (200) reflections. (f), (g) Energy-dispersive x-ray spectroscopy of the 50-nm and 230-nm $Cr:In_2O_3$ films. (h) Schematic illustration of the in-plane lattice matching between $Cr:In_2O_3$ and PMN-PT unit cells.

of the highest In_2O_3 (222) reflection increases with the film thickness [Fig. 1(b)], which is consistent with the cross-section SEM images shown in Fig. 1(c) from which one may find that the crystallite size increases with increasing film thickness from 25 to 230 nm. XRD φ scan measurements are taken on the $Cr:In_2O_3$ (400) and PMN-PT (200) reflections of a 230-nm $Cr:In_2O_3$/PMN-PT structure to establish the in-plane epitaxial relationship between the $Cr:In_2O_3$ film and the PMN-PT substrate. Figure 1(e) shows that the 230-nm $Cr:In_2O_3$ film has two sets of threefold symmetrical reflections and the PMN-PT substrate has only one set of threefold symmetrical reflections, revealing domain-matching epitaxial growth of the $Cr:In_2O_3$ film on the PMN-PT substrate. As schematically shown in Fig. 1(h), the $Cr:In_2O_3$/PMN-PT structure could have two in-plane lattice matching modes: the green solid triangle represents the in-plane orientation relationship $[01\bar{1}]$ $Cr:In_2O_3\|[01\bar{1}]$PMN-PT and $[\bar{2}11]$ $Cr:In_2O_3\|[\bar{2}11]$PMN-PT, while the green hollow one rotates by 60° relative to the solid one within the (111) plane. The cross-section HRTEM image taken at the film-substrate interface confirms the epitaxial growth of the $Cr:In_2O_3$ film on the PMN-PT substrate [Fig. 1(d)]. In addition, the average chromium contents of the 50-nm and 230-nm $Cr:In_2O_3$ films determined by the EDS measurements [Figs. 1(f) and 1(g)] are 2.7 and 2.9%, respectively, close to the nominal Cr-doping level (2.5%) of the target.

Utilizing the experimental setup shown in the inset of Fig. 2(a), the resistance of the $Cr:In_2O_3$ films with different thicknesses is measured at $T = 300$ K by sweeping the electric fields following the sequence $0\ \text{kV/cm} \rightarrow -6.6\ \text{kV/cm} \rightarrow 0\ \text{kV/cm} \rightarrow +6.6\ \text{kV/cm} \rightarrow 0\ \text{kV/cm}$. Note that the coercive fields of the PMN-PT substrates are less than ±3 kV/cm [the inset of Fig. 2(b)]. A maximum electric field of ±6.6 kV/cm is sufficiently large to ensure complete switching of the polarization direction. Whether the PMN-PT is in the fully positive polarized state [i.e., polarization direction points to the $Cr:In_2O_3$ films, denoted as the P_r^+ state and schematically shown in Fig. 2(c)] or the fully negative polarized state [i.e., polarization direction points to the bottom Ag electrode, denoted as the P_r^- state and schematically shown in Fig. 2(c)], the resistance of the films decreases with increasing film thickness [Fig. 2(a)] and could be reversibly switched between the high- and low-resistance states upon switching the polarization state between P_r^+ and P_r^- [Fig. 2(b)], resulting in rectanglelike resistance versus electric field hysteresis loops whose shapes are similar to the ferroelectric hysteresis loop of the PMN-PT substrate shown in the inset of Fig. 2(b). These resistance behaviors are typical characteristics of the ferroelectric field effect, which are explicated in more detail later. As is known, for some PMN-PT-based heterostructures, another regulation mechanism called the lattice-strain effect plays the dominant role [23,24], where the electric-field-induced in-plane strain in PMN-PT substrate is transferred to the film through the interface and thus modulates the strain-related properties of films. To rule out the lattice-strain effect, we perform the XRD measurements of the 110-nm $Cr:In_2O_3$/PMN-PT heterostructure at different polarization states. As shown in Fig. 2(d), the diffraction peaks of the $Cr:In_2O_3$(222) and PMN-PT(111) remain unchanged upon the polarization

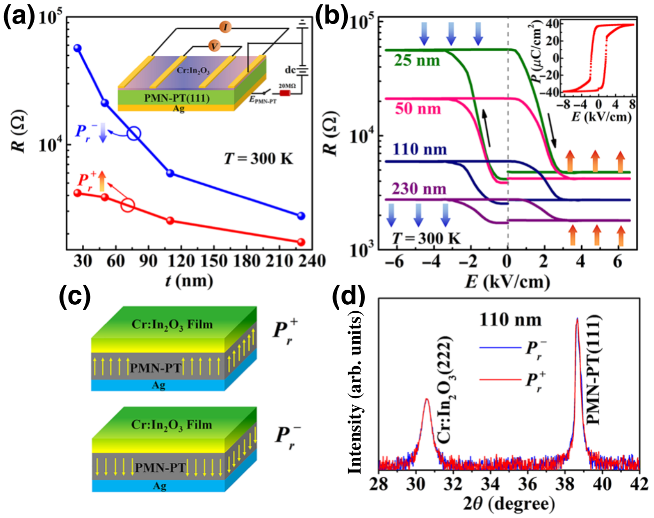

FIG. 2. (a) Resistance of the $Cr:In_2O_3$ films as a function of film thickness for the $P_r{}^+$ and $P_r{}^-$ states of the PMN-PT. Inset: schematic of resistance measurement configuration in which the electric field is applied along the thickness direction of PMN-PT. (b) Resistance of the $Cr:In_2O_3$ films with different thicknesses as a function of the electric field applied to the PMN-PT substrates along the thickness direction. Inset: the ferroelectric *P-E* hysteresis loop of a PMN-PT substrate. (c) Schematic illustrations of the positively polarized $P_r{}^+$ state and the negatively polarized $P_r{}^-$ state. (d) XRD θ–2θ scan patterns for the 110-nm $Cr:In_2O_3$/PMN-PT heterostructure for different polarization states of the PMN-PT.

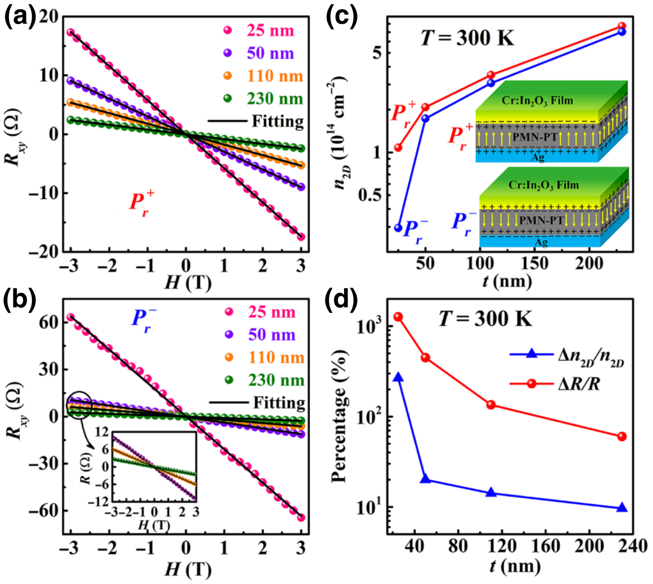

FIG. 3. Hall resistance as a function of the magnetic field for the $Cr:In_2O_3$ films with different thicknesses for the $P_r{}^+$ (a) and $P_r{}^-$ (b) states of the PMN-PT. Inset: the expanded view of the R_{xy} vs H curves of thicker $Cr:In_2O_3$ films for the $P_r{}^-$ state. (c) Areal electron carrier density of the $Cr:In_2O_3$ films with different thicknesses for the $P_r{}^+$ and $P_r{}^-$ states of the PMN-PT. Insets: schematic illustrations of the polarization direction and polarization charges at the top and bottom surfaces of the PMN-PT for the $P_r{}^+$ and $P_r{}^-$ states. (d) Relative areal electron carrier density and resistance changes as a function of film thickness for the $Cr:In_2O_3$ films.

switching from $P_r{}^+$ to $P_r{}^-$. This means that the strain states of the $Cr:In_2O_3$ film and PMN-PT substrate remain unchanged, strongly indicating that the lattice-strain effect fails to account for the large difference in the resistance between the two different polarization states. These results strongly imply that the ferroelectric field effect plays a leading role in the $Cr:In_2O_3$/PMN-PT heterostructures. In addition, due to the existence of the remanent polarization charges on the top surface of the PMN-PT substrates, the resistance of all $Cr:In_2O_3$ films remains stable and nonvolatile even after the $E = +6.6$ or -6.6 kV/cm electric field had been switched off [Fig. 2(b)], which is favorable for nonvolatile memory device applications.

Since the ferroelectric field effect is an interfacial charge-mediated coupling phenomenon, we perform Hall effect measurements on all $Cr:In_2O_3$ films for the two polarization states ($P_r{}^+$ and $P_r{}^-$) of the PMN-PT via the Van der Pauw method. As displayed in Figs. 3(a) and 3(b), regardless of the polarization states, the slopes of the Hall resistance (R_{xy}) versus the magnetic field (H) curves are negative, indicating that the $Cr:In_2O_3$ films are *n*-type semiconductors. We calculate the areal electron carrier density (n_{2D}) of all $Cr:In_2O_3$ films by linear fitting the Hall resistance and show n_{2D} in Fig. 3(c). Upon switching the polarization state from $P_r{}^+$ to $P_r{}^-$, n_{2D} are reduced [Fig. 3(c)] due to the depletion of electron carriers, resulting in an increase in the resistance [Fig. 2(a)]. As schematically illustrated in the inset of Fig. 3(c), the application of positive electric fields to the PMN-PT induces negative polarization charges at the top surface of the PMN-PT, which would extract hole carriers of the film to the interface region to compensate the negative polarization charges. As a result, the electron carrier density increases, resulting in a decrease in the resistance. In contrast, the application of a negative electric field to the PMN-PT depletes electron carriers in the $Cr:In_2O_3$ film, resulting in an increase in the resistance. Using the values of the resistance and areal electron carrier density for the $P_r{}^+$ and $P_r{}^-$ states, we calculate the polarization-switching-induced relative resistance and areal carrier-density changes using $\Delta R/R = [R(P_r{}^-) - R(P_r{}^+)]/R(P_r{}^+)$ and $\Delta n_{2D}/n_{2D} = [n_{2D}(P_r{}^+) - n_{2D}(P_r{}^-)]/n_{2D}(P_r{}^-)$, respectively. It is noteworthy that $\Delta R/R$ reaches the highest value of 1265% at $T = 300$ K for the thinnest 25-nm $Cr:In_2O_3$ film. This value is approximately 4–158 times larger than previously reported thin film- and PMN-PT-based structures, such as the FeRh/PMN-PT ≈ 8% [23], $Bi_{0.94}Pb_{0.06}CuSeO$/PMN-PT ≈ 26% [25], $NdNiO_3$/PMN-PT ≈ 125% [24], and MoS_2/PMN-PT ≈ 332% [26].

Furthermore, both the relative resistance and areal electron carrier-density changes show a decreasing trend with increasing film thickness [Fig. 3(d)], meaning that the regulation efficiency of the ferroelectric field effect on the electronic transport properties is more significant in thinner films. Because the polarization charges have a penetration depth, the farther the thin-film layer is away from the interface, the less the electron carrier density in the layer is affected by the polarization charges. As a result, $\Delta n_{2D}/n_{2D}$ decreases from 266% to 9% with increasing film thickness, leading to a reduction of $\Delta R/R$ [27,28]. From the measured remnant polarization $P_r \approx 40\ \mu\text{C/cm}^2$ for the PMN-PT, the theoretical areal electron carrier-density change (Δ^*_{n2D}) due to the polarization switching is $2P_r/e = 5 \times 10^{14}\ \text{cm}^{-2}$. However, for the 25-nm Cr:In$_2$O$_3$ film with the highest $\Delta n_{2D}/n_{2D}$, the measured actual Δn_{2D} is $1.1 \times 10^{14}\ \text{cm}^{-2}$, much smaller than the theoretical value. It has been reported that the polarization charges can be partly compensated by interface traps and charge traps, thereby suppressing the ferroelectric field effect [16,28–30].

Magnetoresistance is an important quantity to characterize the exchange interactions between charge carriers and local moments and is usually related to the charge carrier density [7,31,32]. The ferroelectric field effect could provide an effective and stringent approach to understand the relationship between the MR and the electron carrier density for the Cr:In$_2$O$_3$/PMN-PT structures since the electron carrier density of the Cr:In$_2$O$_3$ films could be *in situ* modified through the polarization switching of the PMN-PT. Figure 4 shows the MR of all Cr:In$_2$O$_3$ films as a function of the magnetic field applied perpendicular to the film plane for the two polarization states (P_r^+ and P_r^-) of the PMN-PT, as measured at different fixed temperatures

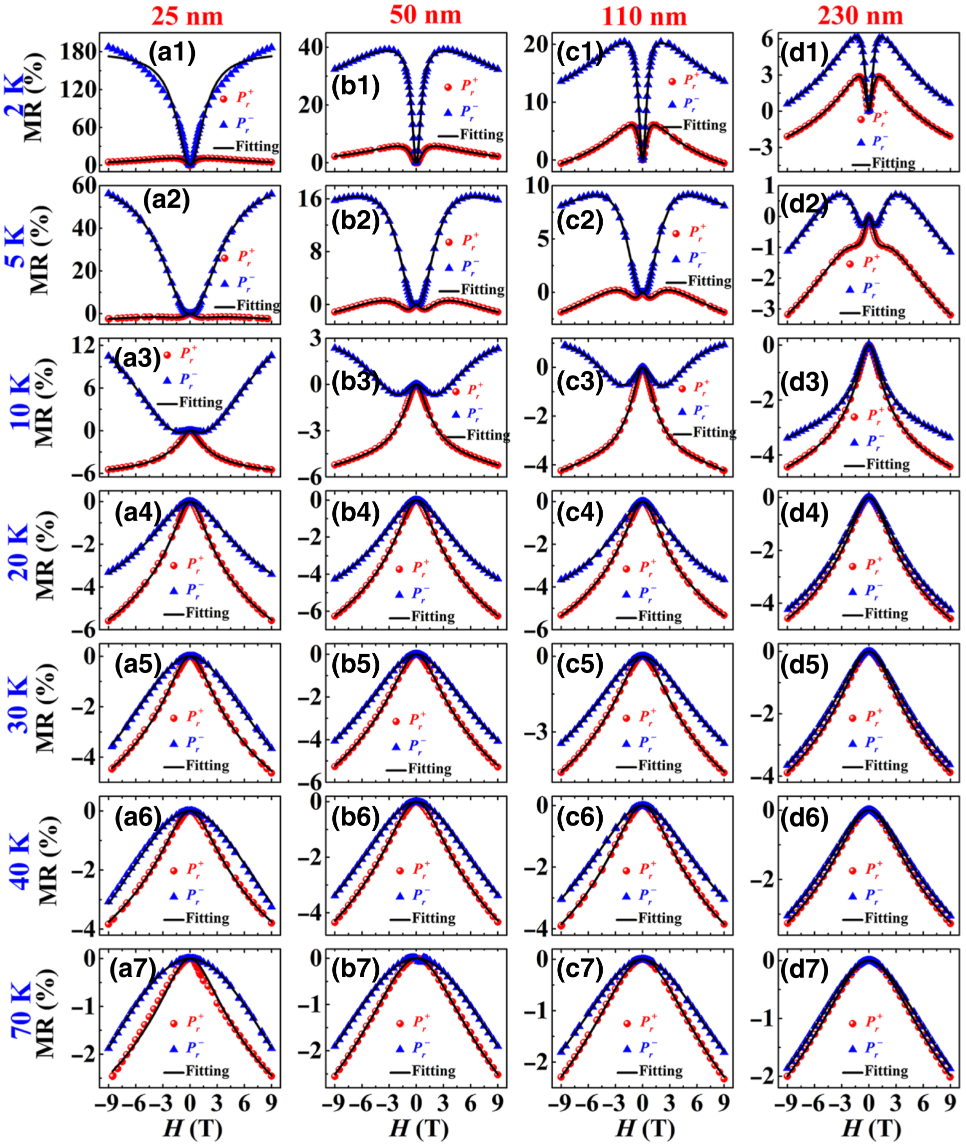

FIG. 4. Magnetoresistance of the Cr:In$_2$O$_3$ films with different thicknesses as a function of the magnetic field H for the P_r^+ and P_r^- states of the PMN-PT, as measured at a fixed temperature ranging from 2–70 K. Black solid lines are the fitting curves.

ranging from 2 to 70 K. Overall, MR shows strong polarization state, film thickness, and temperature-dependent behaviors. At low fixed temperatures (e.g., 2, 5, 10 K), there are strong polarization-switching-induced competitions between PMR and NMR. For instance, upon switching the polarization state from P_r^+ to P_r^- (corresponding to a reduction in the electron carrier density of the Cr:In$_2$O$_3$ films) the PMR is dramatically enhanced [Figs. 4(a1)–(c1), 4(a2)–(c2), 4(a3)–(c3)]. Take $T = 2$ K for an example, upon switching the polarization state from P_r^+ to P_r^-, MR at $H = 9$ T for the thinnest 25-nm Cr:In$_2$O$_3$ film changes from +4.9% to +186.5%, corresponding to an increase in MR by approximately 3706%. Since the ferroelectric field effect is an interfacial phenomenon the polarization-switching-induced change in MR would decrease with increasing film thickness. Indeed, for the thickest 230-nm Cr:In$_2$O$_3$ film the switching of the polarization state from P_r^+ to P_r^- only causes a small change of MR (at $H = 9$ T) from −2.1% to +0.6% . It is interesting that, at $T = 10$ K, for the 25-, 50-, and 110-nm Cr:In$_2$O$_3$ films the polarization switching not only induces reversible and nonvolatile changes in the magnitude of MR but also reversible and nonvolatile changes in the sign of MR [Figs. 4(a3)–4(c3)], which implies strong coupling between the MR and the electron carrier density. As shown in Figs. 4(a1)–4(d1) and 4(a2)–4(d2), as the film thickness increases from 25 to 230 nm, the PMR decreases rapidly. For example, for the P_r^- state and $T = 2$ K, with increasing film thickness from 25 to 230 nm the PMR at $H = 9$ T decreases rapidly from +186.5% for the 25-nm film to +0.6% for the 230-nm one. For another example, for the P_r^- state and $T = 10$ K, the PMR evolves from +10.8% (25 nm) to +2.8% (50 nm) to +1% (110 nm) and finally to −3.2% (230 nm). Moreover, the crossover temperatures from PMR to NMR decreases with increasing film thickness [Figs. 5(e)–5(h)]. All these variations of MR with film thickness could also be due to the increase in the electron carrier density associated with increasing film thickness. Indeed, the Hall effect measurements show that the electron carrier density increases from $0.21 \times 10^{19}/\text{cm}^3$ (2 K) – $1.05 \times 10^{19}/\text{cm}^3$ (70 K) for the 25-nm film to $2.73 \times 10^{19}/\text{cm}^3$ (2 K) – $3.14 \times 10^{19}/\text{cm}^3$ (70 K) for the 230-nm one [insets (I) of Figs. 5(e)–5(h)]. As the temperature is raised to 20 K or above, the PMR is completely quenched while the NMR dominates in the whole magnetic field range from −9 to 9 T for all Cr:In$_2$O$_3$ films with different thicknesses, regardless of the polarization states of the PMN-PT substrates. The NMR is often observed in TM-doped dilute magnetic semiconductors in the weak localization regime when the dimensionless parameter $k_F l > 1$ [9,15]. $k_F l$ can be calculated using the equation $k_F l = \hbar(3\pi^2)^{2/3}/(e^2 \rho n^{1/3})$, where k_F is the Fermi wave vector, l the mean free path, $\hbar$ the Planck constant, e the electron charge, ρ the resistance, and n the volume electron carrier density. However, in our case, the calculated values of $k_F l$ for all films are smaller than 1 [Figs. 5(a)–5(d)], which implies that the films are not in the weak localization regime. Thus, the NMR may not be understood by the magnetic-field-induced suppression of the weak localization. It may be explained by the model proposed by Khosla and Fischer who take the third order *s-d* exchange Hamiltonian of spin scattering by localized moments into account [33,34]. Within the framework of this model the NMR is expressed as

$$\frac{\Delta R}{R(0)} = \frac{R(H) - R(0)}{R(0)} = -a^2 \ln(1 + b^2 H^2), \qquad (1)$$

$$a^2 = A_1 J D(\varepsilon_F) \left[S(S+1) + \langle M^2 \rangle \right], \qquad (2)$$

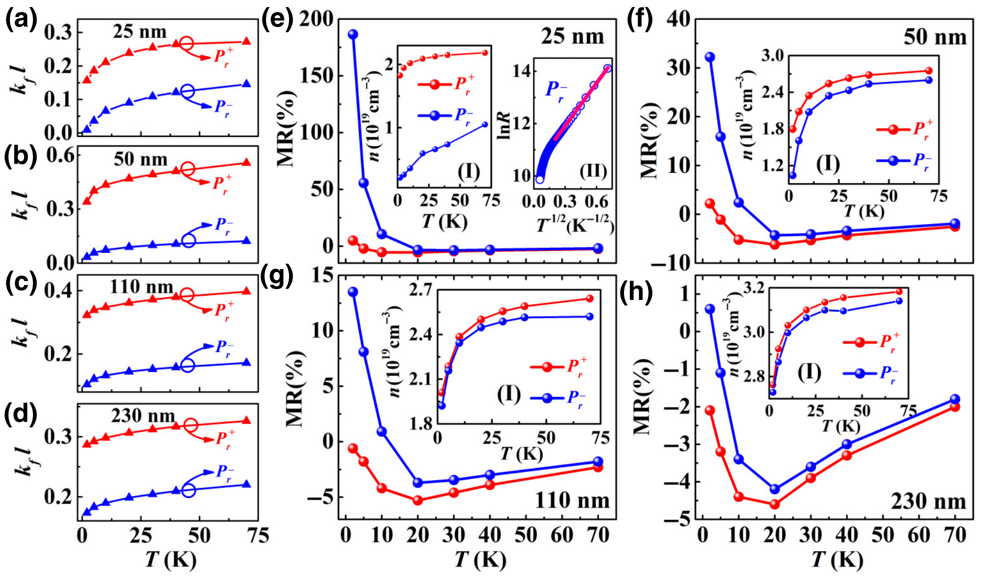

FIG. 5. (a)–(d) Temperature dependence of the dimensionless parameter $k_F l$ for the Cr:In$_2$O$_3$ films with different thicknesses for the P_r^+ and P_r^- states of the PMN-PT. (e)–(h) MR of the Cr:In$_2$O$_3$ thin films at $H = 9$ T as a function of temperature for the P_r^+ and P_r^- states of the PMN-PT. Inset (I): the electron carrier density of the Cr:In$_2$O$_3$ films as a function of temperature for the P_r^+ and P_r^- states of the PMN-PT. Inset (II): the ln$R$ vs $T^{-1/2}$ plot for the 25-nm Cr:In$_2$O$_3$ film for the P_r^- state of the PMN-PT.

$$b^2 = \left\{1 + 4S^2\pi^2\left[\frac{2JD(\varepsilon_F)}{g}\right]^4\right\}\left(\frac{g\mu_B}{\alpha k_B T}\right)^2. \tag{3}$$

Here, H represents the magnetic field intensity, A_1 is the contribution of spin scattering, J is the exchange interaction integral, $D(\varepsilon_F)$ is the density of states at the Fermi level, S is the spin of the localized magnetic moment, $\langle M\rangle$ is the average magnetization, g is the effective Lande factor of the localized magnetic moment, μ_B is the Bohr magneton, α is a numerical constant on the order of unity, and k_B is the Boltzmann constant. On the other hand, the PMR could be explained by employing the two-band model, which is closely related to the charge carrier density and temperature [34,35]. In this model, due to the *s*-*d* exchange interaction, the conduction band splits into two subbands with spin-up and spin-down carriers. The charge carrier density and mobility of charge carriers in the two subbands are influenced by the temperature-dependent spin-splitting effect and thermally activated energy. The two-band model predicts PMR and gives a semiempirical expression [7,35]:

$$\frac{\Delta R}{R(0)} = \frac{c^2H^2}{1 + d^2H^2}, \tag{4}$$

$$c^2 = \frac{\sigma_1\sigma_2\left(\mu_1 + \mu_2\right)^2}{\left(\sigma_1 + \sigma_2\right)^2}, \tag{5}$$

$$d^2 = \frac{\left(\sigma_1\mu_2 - \sigma_2\mu_1\right)^2}{\left(\sigma_1 + \sigma_2\right)^2}, \tag{6}$$

where $\sigma_1(\sigma_2)$ and $\mu_1(\mu_2)$ are the conductivity and mobility of carriers in the majority (minority) band. Therefore, the parameters c and d are functions of carrier density and carrier mobility in the two bands. The PMR is proportional to H^2 at low fields whereas saturates at high fields.

The total MR is a superposition of the PMR and NMR and can be expressed as a combination of Eqs. (1) and (4):

$$\frac{\Delta R}{R(0)} = -a^2\ln(1 + b^2H^2) + \frac{c^2H^2}{1 + d^2H^2}. \tag{7}$$

Since the PMR for all films with different thicknesses are completely quenched when the temperature is 20 K and above, regardless of the polarization states of the PMN-PT, we thus fit the MR for $T \geq 20$ K using Eq. (1) while that for $T < 20$ K using Eq. (7). As shown in Fig. 4, for all Cr:In$_2$O$_3$ films with different thicknesses, the MR for different temperatures and polarization states of the PMN-PT can be quite well fitted using the parameters listed in Table I (except the PMR at 2 K for the 25-nm Cr:In$_2$O$_3$ film for the P_r^- state), which demonstrates that the present description of the MR behaviors at different temperatures for different film thicknesses and polarization states of the PMN-PT using the above models is valid on the whole. We note that for the P_r^- state the 25-nm Cr:In$_2$O$_3$ film shows a large nonsaturating PMR up to 186.5% at 2 K [Fig. 4(a1)]. Similar phenomena have also been observed in TM-doped ZnO and In$_2$O$_3$ films in the VRH regime [6,13,14]. As shown in inset (II) of Fig. 5(e), for the P_r^- state, the 25-nm Cr:In$_2$O$_3$ film shows a linear relationship between ln$R$ and $T^{-1/2}$ at low temperatures, which indicates that the electronic transport at low temperatures follows the VRH mechanism. Moreover, Figs. 5(a)–5(d) reveal that the values of k_Fl for the P_r^- state are much smaller than those for the P_r^+ state, indicating that the electron carriers are more localized for the P_r^- state. In particular, for the 25-nm Cr:In$_2$O$_3$ film for the P_r^- state and $T = 2$ K, k_Fl is only 0.009, which implies that the electron carriers are highly localized. In the VRH regime with highly localized electron carriers and at a sufficiently low temperature (e.g., 2 K), a large PMR would appear due to the shrinking of the wave functions of states available for an electron hop [6,13,14] and could be described by $\ln[\rho(H)/\rho(0)] \propto H^n$ from which one may expect that the PMR is nonsaturating at high magnetic fields, consistent with the experimental results.

Table I lists the values of the fitting parameters a, b, c, d for all Cr:In$_2$O$_3$ films. According to Eq. (3), the parameter b is inversely proportional to the temperature T, which has been regarded as an evidence for this MR mechanism [31,34]. As shown in Fig. 6, there is a $1/T$ linearity of the parameter b for all films in the temperature range from 10 to 70 K for the two polarization states (P_r^+ and P_r^-) of the PMN-PT. With increasing temperature from 2 to 20 K the PMR vanishes, which enables us to observe the variation of the NMR with temperature more clearly. As can be seen in Figs. 5(e)–5(h), the NMR gradually diminishes as the temperature increases from 20 to 70 K, which is consistent with the decrease in the parameter b with increasing temperature from 20 to 70 K (Fig. 6). In the model proposed by Khosla and Fischer, the NMR originates from the reduced spin scattering of conducting electrons because the localized spins tend to be aligned parallel in magnetic fields. Increasing temperature causes progressive randomization of the orientation of localized spins, which suppresses NMR [36]. Furthermore, at a fixed temperature for $T \geq 20$ K, upon switching the polarization state from P_r^- to P_r^+, the NMR for all films increases as the carrier density increases, which implies that a higher electron carrier density favors a stronger coupling between electron carriers and local moments and thus leads to a larger NMR. On the other hand, the PMR shows a much stronger temperature and carrier-density-dependent behaviors than the NMR does. As shown in Figs. 5(e)–5(h), the PMR of all Cr:In$_2$O$_3$ films decreases rapidly with increasing temperature from 2 to 10 K and changes to NMR at 20 K, which is also reflected

TABLE I. Values of the fitting parameters *a*, *b*, *c*, *d* obtained from least-squares fits of MR data [the data at the temperatures of 2, 5, and 10 K are fitted using Eq. (7); the data at the temperatures of 20, 30, 40, and 70 K are fitted using Eq. (1)].

	T (K)	a (P_r^+)	b (P_r^+)	c (P_r^+)	d (P_r^+)	a (P_r^-)	b (P_r^-)	c (P_r^-)	d (P_r^-)
25 nm	2	1.947	0.3122	6.573	1.802				
	5	1.227	2.123	0.988	0.3917	0.7237	5.653	2.253	0.2689
	10	1.154	1.339	0.1554	0.0841	1.009	0.8094	0.642	0.1276
	20	1.201	0.7124			1.195	0.3664		
	30	1.214	0.5405			1.7	0.1912		
	40	1.181	0.439			1.668	0.1582		
	70	0.9303	0.3563			1.753	0.0978		
50 nm	2	1.382	0.5475	3.607	1.235	2.791	0.1143	10.84	1.638
	5	1.469	1.653	1.61	0.483	1.827	1.386	2.59	0.4456
	10	1.25	1.162	0.2805	0.1573	1.273	0.717	0.6105	0.1697
	20	1.315	0.6458			1.259	0.4052		
	30	1.335	0.4672			1.484	0.2555		
	40	1.296	0.3816			1.534	0.1983		
	70	1.186	0.2472			1.473	0.1127		
110 nm	2	1.606	0.635	5.878	2.014	2.09	0.3145	9.147	1.931
	5	1.378	1.706	1.602	0.5456	1.596	1.437	2.347	0.5045
	10	1.148	1.192	0.3005	0.1735	1.127	0.8415	0.5349	0.1841
	20	1.204	0.6964			1.084	0.5058		
	30	1.231	0.4746			2.021	0.3069		
	40	1.211	0.3782			1.305	0.2406		
	70	1.106	0.2487			1.244	0.1649		
230 nm	2	1.366	0.696	4.137	1.984	1.521	0.5797	5.514	1.903
	5	1.243	1.695	1.201	0.5407	1.37	1.489	1.554	0.5132
	10	1.051	1.128	0.1584	0.1466	1.017	0.9997	0.236	0.1767
	20	1.139	0.6269			1.156	0.5337		
	30	1.157	0.4436			1.207	0.3696		
	40	1.137	0.3602			1.202	0.306		
	70	1.07	0.2416			1.113	0.2066		

by the significant decrease in the fitting parameters *c* with increasing temperature (Table I). With increasing temperature from 2 to 10 K the electron carrier density increases [insets (I) of Figs. 5(e)–5(h)], making the Femi energy larger than the spin-splitting energy. As a result, the spin-splitting decays rapidly, leading to a decrease in the PMR [5,7,32]. Similarly, switching the polarization state from P_r^- to P_r^+ also induces an increase in the electron carrier density, which would lead to a decay of the spin splitting and thus a decrease in the PMR. Moreover, it is noteworthy that, at a certain low temperature (e.g., 10 K), MR for the 25-nm Cr:In_2O_3 film could be *in situ* converted from positive (+10.5%) to negative (−5.5%) by switching the polarization state from P_r^- to P_r^+, which can be explained by a significant decrease in the spin-splitting effect due to the increase in the electron carrier density, as a result, the PMR is completely suppressed and the NMR appears for the P_r^+ state [7,32,37]. In a similar way, the NMR could be switched back to PMR by switching the polarization state from P_r^+ to P_r^-. Namely, the switching of the MR between positive and negative is reversible and nonvolatile due to the reversible and nonvolatile modulation of the electron carrier density via the ferroelectric field effect.

Using Eqs. (1), (4), and (7), both PMR and NMR can be disentangled into positive and negative components, respectively. Hereafter, the positive and negative components are referred to as MR(+) and MR(−), respectively.

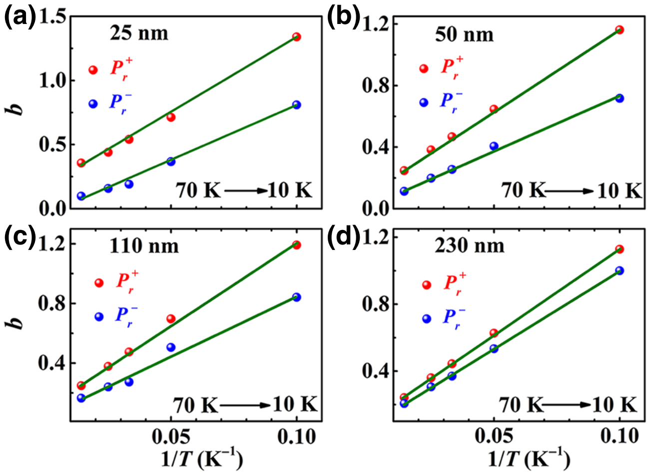

FIG. 6. Fitting parameter *b* as a function of the inverse temperature for the Cr:In_2O_3/PMN-PT structures with different film thicknesses.

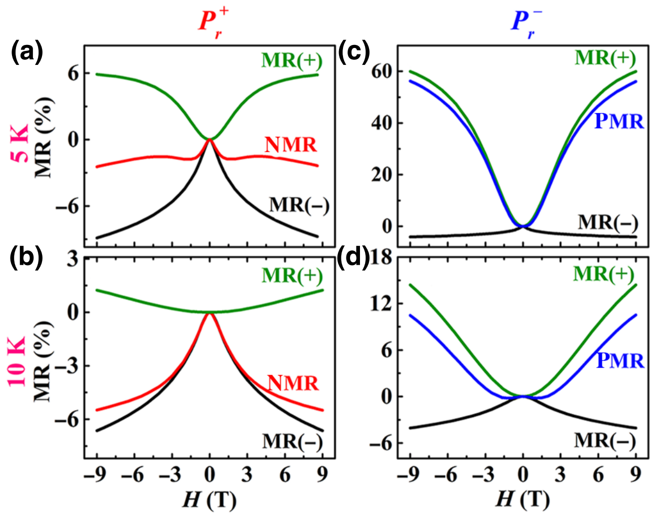

FIG. 7. Experimentally measured positive MR and negative MR and the disentangled MR(+) and MR(−) components using Eq. (7) for the 25-nm Cr:In$_2$O$_3$ film for the P_r^+ and P_r^- states of the PMN-PT at a fixed temperature of 5 K (a,c) and 10 K (b,d).

We plotted the MR(+) and MR(−) as well as the PMR and NMR of the 25-nm Cr:In$_2$O$_3$ film for $T = 5$ and 10 K and P_r^+ and P_r^- states of the PMN-PT in Fig. 7. Firstly, we analyze the effects of temperature on MR(+) and MR(−). For the P_r^+ state and $T = 5$ K, both the MR(+) and the MR(−) contribute to the NMR with the latter slightly larger than the former, thereby resulting in a small NMR of approximately −2.4% at $H = 9$ T [Fig. 7(a)]. As the temperature is raised from 5 to 10 K, the MR(−) decreases from −8.7% to −6.6% while the MR(+) decreases significantly from +5.9% to +1.2% [Fig. 7(b)], resulting in a larger NMR of approximately −5.5% at $H = 9$ T. These results indicate that the increase in the NMR with increasing temperature is mainly due to the decrease in the MR(+). Similarly, for the P_r^- state and $T = 5$ K both the MR(+) and the MR(−) contribute to the PMR with the former (+60.0%) much larger than the latter (−4.1%), resulting in a large PMR of approximately +56.1% at $H = 9$ T [Fig. 7(c)]. As the temperature is raised from 5 to 10 K, the MR(−) still remains as −4.1% while the MR(+) decreases significantly from +60.0% to +14.4% [Fig. 7(d)], thereby significantly reducing the PMR from +56.1% to +10.5% at $H = 9$ T. These results demonstrate that the decrease in the PMR with increasing temperature is also mainly due to the decrease in the MR(+). Now, we turn to the effects of polarization switching on the MR(+) and MR(−). At $T = 5$ K, upon switching the polarization state from P_r^- to P_r^+ (corresponding to an increase in the electron carrier density), the MR(+) decreases significantly from +60.0% to +5.9% while the MR(−) only slightly changes from −4.1% to −8.7% at $H = 9$ T [Fig. 5(a) and 5(b)], implying that the polarization-switching-induced change of the sign of MR from positive to negative (i.e., from PMR to NMR) is mainly due to the decrease in the MR(+). Similarly, at $T = 10$ K, upon switching the polarization state from P_r^- to P_r^+ the change of the sign of MR from positive to negative is also mainly due to the rapid decrease of the MR(+) from 14.4% to 1.2% at $H = 9$ T since the MR(−) only slightly changes from −4.1% to −6.6%. All of the above results strongly demonstrate that the positive component of MR [MR(+)] is much more sensitive to the electron carrier density than the MR(−) and plays a dominant role in determining the magnitude and sign of MR of the Cr:In$_2$O$_3$ films.

IV. CONCLUSIONS

In summary, Cr-doped In$_2$O$_3$ semiconductor thin films with thicknesses ranging from 25 to 230 nm have been epitaxially grown on the (111)-oriented ferroelectric PMN-PT single-crystal substrates to form ferroelectric-field-effect devices that enable an *in situ* tuning of the areal electron carrier density (n_{2D}) of the films up to 266% in a reversible and nonvolatile manner. As a result of such a large change in n_{2D}, not only the resistance but also the magnitude and sign of the magnetoresistance could be dramatically modified. For the thinnest 25-nm Cr:In$_2$O$_3$ film the polarization switching results in a reversible and nonvolatile change of the resistance by 1265% at room temperature and a reversible and nonvolatile change of the MR by 3706% at $T = 2$ K and $H = 9$ T. For a certain temperature (e.g., $T = 10$ K) the polarization-switching-induced change in n_{2D} causes reversible and nonvolatile changes in the magnitude and sign of MR, revealing strong coupling between the MR and the electron carrier density. For $T \geq 20$ K, MR is negative regardless of film thickness, temperature, and polarization states of PMN-PT and is enhanced upon increasing the electron carrier density, implying that a higher electron carrier density favors a stronger coupling between electron carriers and local moments. Moreover, we find that MR for both two polarization states (P_r^+ and P_r^-) can be disentangled into positive component [MR(+)] and negative component [MR(−)], respectively. Further, we reveal that the polarization-switching-induced decrease or increase in the positive MR and the change of the sign of MR mainly originates from the rapid decrease or increase in the MR(+), which is caused by the suppression of the spin-splitting effect due to the increase in electron carrier density. More specifically, MR(+) is much more sensitive to the electron carrier density than MR(−), demonstrating the coupling between MR(+) and electron carrier density controls the magnitude and sign of MR. Our systematical results not only provide a comprehensive insight into the intrinsic relationship between MR and electron carrier density, but also demonstrate the great potential of ferroelectric field effect to tune the carrier-density-related properties of semiconductor films, which could be helpful for the design of semiconductor and ferroelectric based nonvolatile spintronic devices.

ACKNOWLEDGMENTS

This work is supported by the National Natural Science Foundation of China (Grants No. 11974155 and No. 51872278).

[1] F. P. Sabino, S.-H. Wei, and A. Janotti, Enabling visible-light absorption and p-type doping in In_2O_3 by adding Bi, Phys. Rev. Mater. **3**, 034605 (2019).

[2] O. Zandi, A. Agrawal, A. B. Shearer, L. C. Reimnitz, C. J. Dahlman, C. M. Staller, and D. J. Milliron, Impacts of surface depletion on the plasmonic properties of doped semiconductor nanocrystals, Nat. Mater. **17**, 710 (2018).

[3] Y.-H. Kim, J. S. Kim, and T.-W. Lee, Strategies to improve luminescence efficiency of metal-halide perovskites and light-emitting diodes, Adv. Mater. **31**, 1804595 (2019).

[4] L. He, T. E. Wood, B. Wu, Y. Dong, L. B. H. L, M. Reyes, D. Wang, C. Kübel, C. Qian, J. Jia, K. Liao, P. G. O'Brien, A. Sandhel, J. Y. Y. Loh, P. Szymanski, N. P. Kherani, T. C. Sum, C. A. Mims, and G. A. Ozin, Spatial separation of charge carriers in $In_2O_{3-x}(OH)_y$ nanocrystal superstructures for enhanced gas-phase photocatalytic activity, ACS Nano **10**, 5578 (2016).

[5] Y. An, Y. Ren, D. Yang, Z. Wu, and J. Liu, Oxygen vacancy-induced room temperature ferromagnetism and magnetoresistance in Fe-doped In_2O_3 films, J. Phys. Chem. C **119**, 4414 (2015).

[6] G. Z. Xing, J. B. Yi, F. Yan, T. Wu, and S. Li, Positive magnetoresistance in ferromagnetic Nd-doped In_2O_3 thin films grown by pulse laser deposition, Appl. Phys. Lett. **104**, 202411 (2014).

[7] Y.-F. Tian, Y.-F. Li, and T. Wu, Tuning magnetoresistance and exchange coupling in ZnO by doping transition metals, Appl. Phys. Lett. **99**, 222503 (2011).

[8] Q. Xu, L. Hartmann, H. Schmidt, H. Hochmuth, M. Lorenz, R. S. Grund, C. Sturm, D. Spemann, and M. Grundmann, Metal-insulator transition in Co-doped ZnO: Magnetotransport properties, Phys. Rev. B **73**, 205342 (2006).

[9] Q. Xu, L. Hartmann, and H. Schmidt, , *s-d* exchange interaction induced magnetoresistance in magnetic ZnO, Phys. Rev. B **76**, 134417 (2007).

[10] N. Jedrecy, M. Hamieh, C. Hebert, and J. Perriere, High magnetoresistance at low magnetic fields in self-assembled ZnO–Co nanocomposite films, Nanoscale **9**, 10431 (2017).

[11] P. Stamenov, M. Venkatesan, L. S. Dorneles, D. Maude, and J. M. D. Coey, Magnetoresistance of Co-doped ZnO thin films, J. Appl. Phys. **99**, 08M124 (2006).

[12] Y. Tian, W. Lin, and T. Wu, Anisotropic Magnetoresistance and Weak Spin-Orbital Coupling in Doped ZnO Thin Films, Phys. Rev. Appl. **100**, 052408 (2012).

[13] Y. F. Tian, S.-S. Yan, Q. Cao, J. X. Deng, Y. X. Chen, G. L. Liu, L. M. Mei, and Y. Qiang, Origin of large positive magnetoresistance in the hard-gap regime of epitaxial Co-doped ZnO ferromagnetic semiconductors, Phys. Rev. B **79**, 115209 (2009).

[14] N. Sharma, S. Granville, S. C. Kashyap, and J.-P. Ansermet, Low-temperature hopping and absence of spin-dependent transport in single crystals of cobalt-doped ZnO, Phys. Rev. B **82**, 125211 (2010).

[15] T. Dietl, T. Andrearczyk, A. Lipińska, M. Kiecana, M. Tay, and Y. Wu, Origin of ferromagnetism in $Zn_{1-x}Co_xO$ from magnetization and spin-dependent magnetoresistance measurements, Phys. Rev. B **76**, 155312 (2007).

[16] A. Rajapitamahuni, L. L. Tao, Y. Hao, J. Song, X. Xu, E. Y. Tsymbal, and X. Hong, Ferroelectric polarization control of magnetic anisotropy in $PbZr_{0.2}Ti_{0.8}O_3/La_{0.8}Sr_{0.2}MnO_3$ heterostructures, Phys. Rev. Mater. **3**, 021401(R) (2019).

[17] J. Hoffman, X. Pan, J. W. Reiner, F. J. Walker, J. P. Han, C. H. Ahn, and T. P. Ma, Ferroelectric field effect transistors for memory applications, Adv. Mater. **22**, 2957 (2010).

[18] A. Malashevich, M. S. J. Marshall, C. Visani, A. S. Disa, H. Xu, F. J. Walker, C. H. Ahn, and S. I. Beigi, Controlling mobility in perovskite oxides by ferroelectric modulation of atomic-scale interface structure, Nano Lett. **18**, 573 (2018).

[19] A. Laudari, A. R. Mazza, A. Daykin, S. Khanra, K. Ghosh, F. Cummings, T. Muller, P. F. Miceli, and S. Guha, Polarization Modulation in Ferroelectric Organic Field-Effect Transistors, Phys. Rev. Appl. **10**, 014011 (2018).

[20] Q.-X. Zhu, M.-M. Yang, M. Zheng, R.-K. Zheng, L.-J. Guo, Y. Wang, J.-X. Zhang, X.-M. Li, H.-S. Luo, and X.-G. Li, Ultrahigh tunability of room temperature electronic transport and ferromagnetism in dilute magnetic semiconductor and PMN-PT single-crystal-based field effect transistors via electric charge mediation, Adv. Funct. Mater. **25**, 1111 (2015).

[21] A. Wang, M. Feng, W. Wang, H. Li, X. Zhao, H. Xu, H. Ke, and Y. Zhou, Influence of composition ratio on ferroelectric, magnetic and magnetoelectric properties of PMN–PT/CFO composite thin films, J. Mater. Sci.: Mater. Electron. **29**, 10164 (2018).

[22] H. J. Lee, S. Zhang, J. Luo, F. Li, and T. R. Shrout, Thickness-dependent properties of relaxor-$PbTiO_3$ ferroelectrics for ultrasonic transducers, Adv. Funct. Mater. **20**, 3154 (2010).

[23] Y. Lee, Z. Q. Liu, J. T. Heron, J. D. Clarkson, J. Hong, C. Ko, M. D. Biegalski, U. Aschauer, S. L. Hsu, M. E. Nowakowski, J. Wu, H. M. Christen, S. Salahuddin, J. B. Bokor, N. A. Spaldin, D. G. Schlom, and R. Ramesh, Large resistivity modulation in mixed-phase metallic systems, Nat. Commun. **6**, 5959 (2015).

[24] J.-M. Yan, M. Xu, T.-W. Chen, M.-M. Yang, F. Liu, H. Wang, L. Guo, Z.-X. Xu, F.-Y. Fan, G.-Y. Gao, S.-N. Dong, X.-G. Li, H.-S. Luo, W. Zhao, and R.-K. Zheng, Manipulation of the Electronic Transport Properties of Charge-Transfer Oxide Thin Films of $NdNiO_3$ Using Static and Electric-Field-Controllable Dynamic Lattice Strain, Phys. Rev. Appl. **11**, 034037 (2019).

[25] X.-W. Zhao, G.-Y. Gao, J.-M. Yan, L. Chen, M. Xu, W.-Y. Zhao, Z.-X. Xu, L. Guo, Y.-K. Liu, X.-G. Li, Y. Wang, and R.-K. Zheng, Reversible and nonvolatile ferroelectric control of two-dimensional electronic transport properties of ZrCuSiAs-type copper oxyselenide thin films with a layered structure, Phys. Rev. Mater. **2**, 055003 (2018).

[26] Y. Liu, J. Guo, A. Yu, Y. Zhang, J. Kou, K. Zhang, R. Wen, Y. Zhang, J. Zhai, and Z. L. Wang, Magnetic-induced-piezopotential gated MoS_2 field-effect transistor at room temperature, Adv. Mater. **14**, 17044524 (2018).

[27] H. Yamada, M. Marinova, P. Altuntas, A. Crassous, L. B. Lours, S. Fusil, E. Jacquet, V. Garcia, K. Bouzehouane, A. Gloter, J. E. Villegas, A. Barthélémy, and M. Bibes, Ferroelectric control of a mott insulator, Sci. Rep. **3**, 2834 (2003).

[28] S. Sanctis, J. Krausmann, C. Guhlb, and J. Schneider, Stacked indium oxide/zinc oxide heterostructures as semiconductors in thin film transistor devices: A case study using atomic layer deposition, J. Mater. Chem. C **6**, 464 (2018).

[29] T. Zhao, S. R. Shinde, S. B. Ogale, H. Zheng, T. Venkatesan, R. Ramesh, and S. D. Sarma, Electric Field Effect in Diluted Magnetic Insulator Anatase Co: TiO_2, Phys. Rev. Lett. **94**, 126601 (2005).

[30] G. Chen, C. Song, C. Chen, S. Gao, F. Zeng, and F. Pan, Resistive switching and magnetic modulation in cobalt-doped ZnO, Adv. Mater. **24**, 3515 (2018).

[31] M. Gacic, G. Jakob, C. Herbort, and H. Adrian, Magnetism of Co-doped ZnO thin films, Phys. Rev. B **75**, 205206 (2007).

[32] S. Ye, V. Ney, T. Kammermeier, K. Ollefs, S. Zhou, H. Schmidt, F. Wilhelm, A. Rogalev, and A. Ney, Absence of ferromagnetic-transport signatures in epitaxial paramagnetic and superparamagnetic $Zn_{0.95}Co_{0.05}O$ film, Phys. Rev. B **80**, 245321 (2009).

[33] R. P. Khosla and J. R. Fischer, Magnetoresistance in degenerate CdS: Localized magnetic moments, Phys. Rev. B **2**, 4084 (1970).

[34] F. Reuss, S. Frank, C. Kirchner, R. Kling, and T. Gruber, Magnetoresistance in epitaxially grown degenerate ZnO thin films, Appl. Phys. Lett. **87**, 112104 (2005).

[35] R. P. Khosla and J. R. Fischer, Low-temperature magnetoresistance in degenerate n-type Si, Phys. Rev. B **6**, 4073 (1972).

[36] S. Kumar, W. Paschoal, A. Johannes, D. Jacobsson, C. Borschel, A. Pertsova, C.-H. Wang, M.-K. Wu, C. M. Canali, C. Ronning, L. Samuelson, and H. Pettersson, Magnetic polarons and large negative magnetoresistance in GaAs nanowires implanted with Mn ions, Nano Lett. **13**, 5079 (2013).

[37] Q. Xu, L. Hartmann, H. Schmidt, H. Hochmuth, M. Lorenz, R. S. Grund, C. Sturm, D. Spemann, and M. Grundmann, Magnetoresistance and anomalous Hall effect in magnetic ZnO films, J. Appl. Phys. **101**, 063908 (2007).